Cell Reports, Volume *22*

Supplemental Information

Glia Modulate a Neuronal Circuit for Locomotion Suppression during Sleep in *C. elegans*

Menachem Katz, Francis Corson, Shachar Iwanir, David Biron, and Shai Shaham

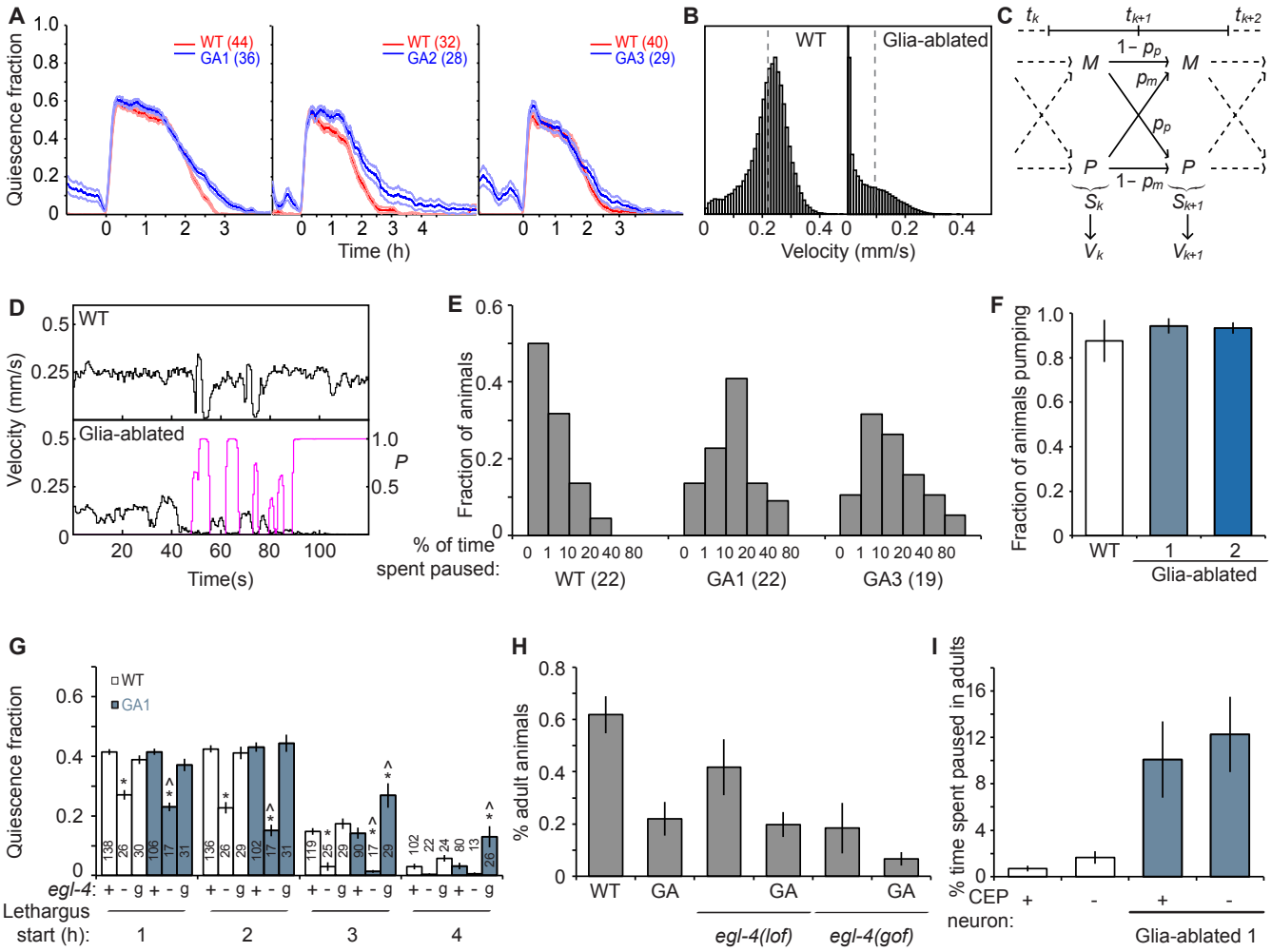

Figure S1. Related to Figure 1.

(A) Average quiescence fraction prior and during lethargus. WT, wild type. GA, glia ablated. Error bars indicate standard error. Number of animals is indicated in each panel.

(B) Velocity distribution of wild-type (WT) and glia-ablated worms.

(C) Hidden Markov Model for worm movement. S_k denotes the state of the worm (moving, *M*, or paused, *P*) in the time interval $[t_k, t_{k+1}]$ between frames *k* and *k*+1. The probabilities of transitions between the two states at each time step are shown by arrows. In each interval between two frames, the hidden state S_k determines the distribution of the observable velocity, V_k.

(D) Analysis of pausing from velocity curves. The instantaneous velocity of the animal is shown in black and the probability that the animal is paused in magenta. (Top) Wild-type worm (WT). Short periods of low velocity (corresponding to reversals and omega-turns) are not identified as pauses. (Bottom) Glia-ablated animal. The animal is initially moving then enters an extended period of pausing. As is often observed, short periods of pausing and slow movement alternate before an extended pause.

(E) Distribution of the percentage of time individual animals are pausing. Number of animals tested is indicated in parentheses below the graph.

(F) CEPsh glia ablation does not inhibit pumping in adults (four repeats).

(G) EGL-4 mutants affect the magnitude of sleep in wild type (WT) and glia-ablated (GA1) animals. *egl-4* loss-of-function mutation, -, gain-of-function mutation, g. Number of animals indicated inside or above bars.

(H) Percent animals reaching adulthood 52 hours after embryos are laid. Experiments are done in triplicate.

(I) Ablation of CEP neurons (-) does not induce locomotory pauses, nor does it suppress pausing of CEPsh-ablated animals (n=2 movies each). Vertical axis, the percentage of total time animals spent pausing out of the total duration of all recorded tracks.

(F-I) Graphs, mean ± s.e.m.; (G) ANOVA Tukey's HSD post hoc test, * compared to WT, ^ compared glia-ablated parent, $p<0.05$.

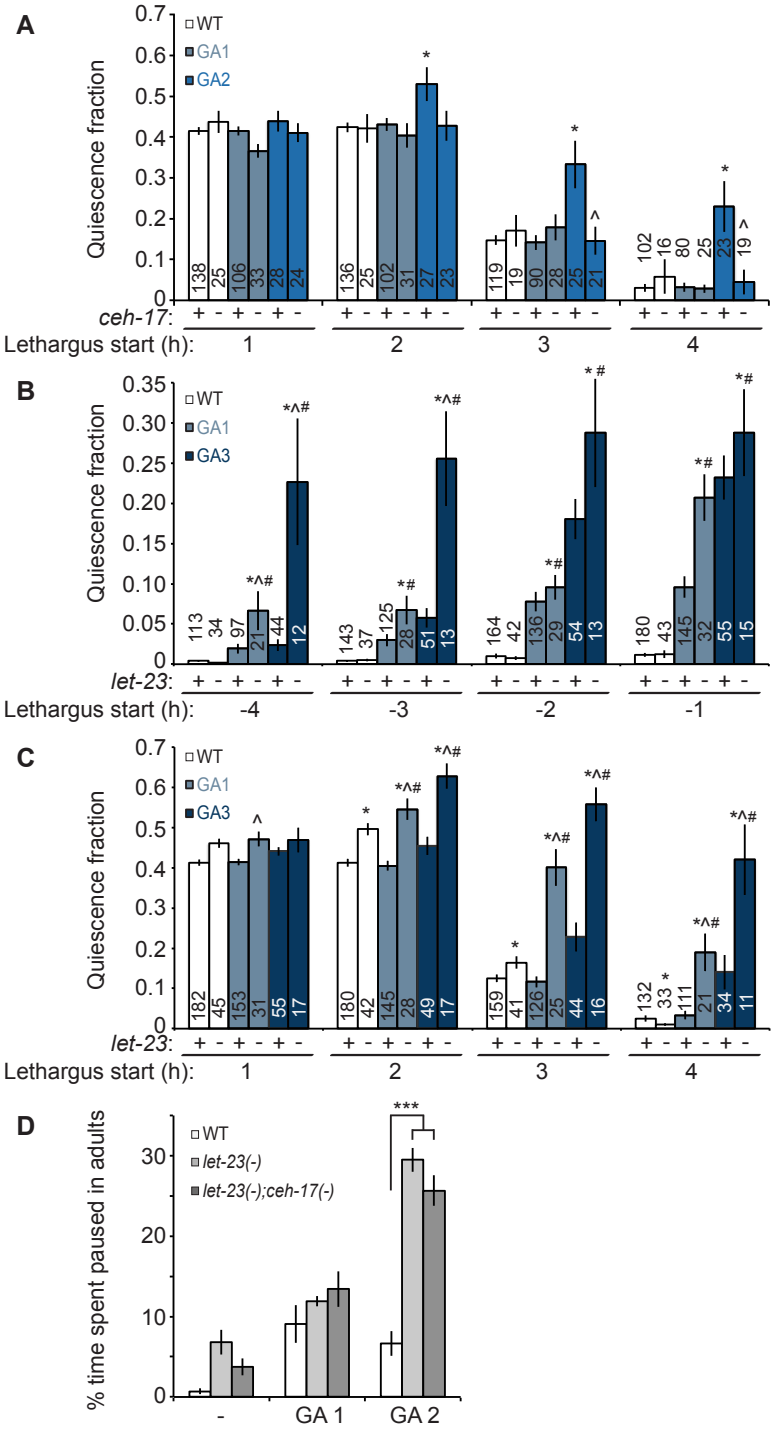

Figure S2. Related to Figure 2.

(A) *ceh-17* mutant **(-)** can rescue enhanced lethargus of CEPsh glia-ablated (GA) animals. Number of animals is indicated inside or above bars.

(B-D) A *let-23* mutation (-) enhances sleep defects of CEPsh glia-ablated animals before (B) and after (C) entry into lethagus, as well as pausing (D; n= 4 movies). Bar graphs, mean ± s.e.m.; ANOVA Tukey's HSD post hoc test, ***** compared to WT, ^ compared glia-ablated parent*,* # compered to parental mutant; number of symbols represent (1) $p<0.05$, (3) $p<0.0005$.

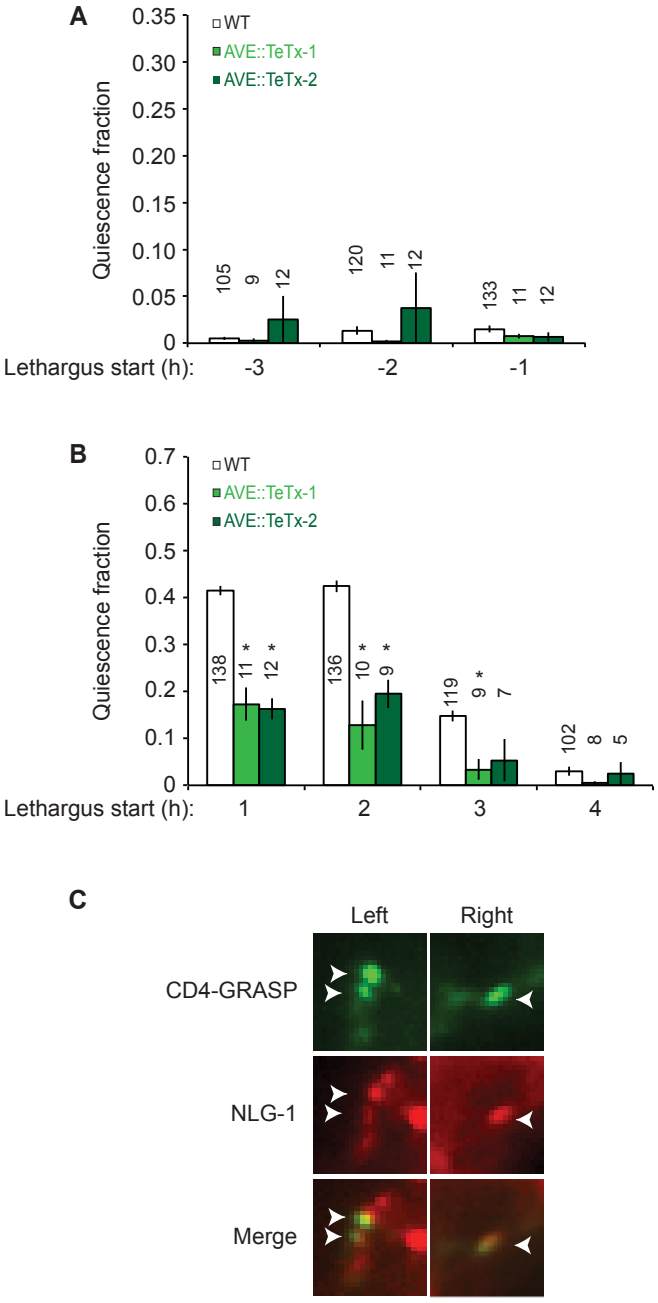

Figure S3. Related to Figure 3.

(A) Inhibition of AVE does not affect entry into lethargus. Number of animals is indicated above bars.

(B) AVE inhibition reduces lethargus quiescence. Number of animals is indicated inside or above bars.

(A,B) Bar graphs, mean ± s.e.m.; ANOVA Tukey's HSD post hoc test, * compared to WT, $p<0.05$.

(C) ALA-AVE synaptic contacts are maintained in CEPsh glia-ablated animals. ALA expresses CD4::spGFP11, and AVE expresses CD4::spGFP1-10, inactive GFP fragments that fluoresce when in close contact. Green signal corresponds to sites of contact. Neuroligin marks post-synaptic sites on AVE in red (NLG-1::mCherry). Synapses on both the left and the right sides of the nerve ring are presented.

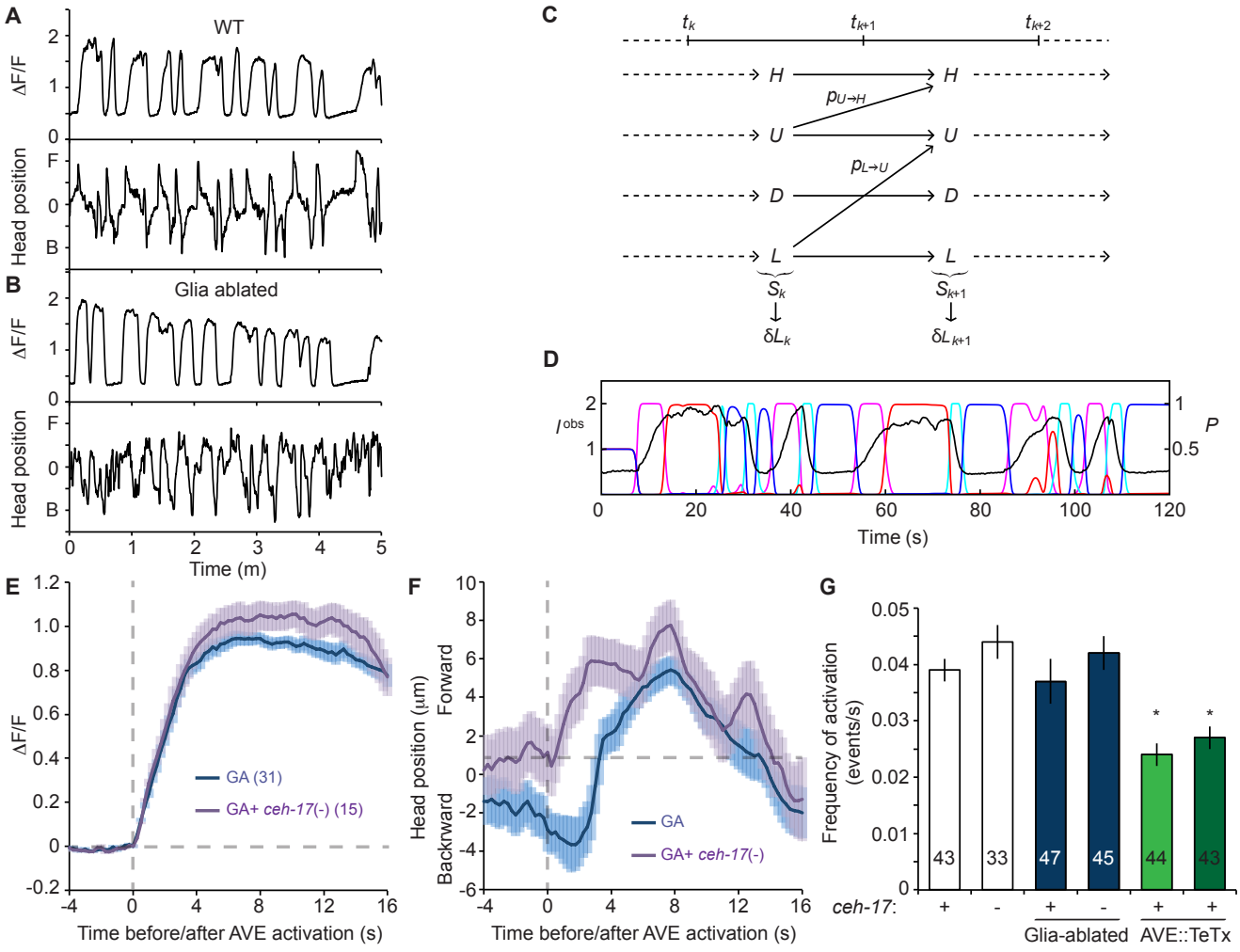

Figure S4. Related to Figure 4.

(A,B) Representative 5 minute recording of spontaneous GCaMP signals (top; Intensity/average intensity) and of head position (bottom), from a wild-type (WT; A) and a CEPsh glia-ablated animal (B).

(C) Hidden Markov Model for the analysis of neuron activity. The model comprises four activitystates, ramping up (*U*), ramping down (*D*), high plateau (*H*), and low plateau (*L*). The activity state S_k of the neuron in the time interval $[t_k, t_{k+1}]$ determines the distribution of the step δL_k in activity level between times t_k and t_{k+1}. For the sake of legibility, only two of the possible transitions between distinct activity states are shown, corresponding to the onset of neuron activity ($L \to U$) and to the stabilization of activity at a high level ($U \to H$). Some transitions (e.g. $U \to L$) are not permitted, in accordance with the natural meaning of the four activity states (only a decrease in activity can terminate in the low plateau state).

(D) Classification of activity states using a Hidden Markov Model. The measured activity level is plotted in black, while the colored curves show the probability of the different activity states, ramping up (magenta), ramping down (cyan), high plateau (red), and low plateau (dark blue).

(E,F) Average of AVE GCaMP signals (E), and head position (F) recorded from animals showing error responses. Dashed gray line, GCaMP signal rise initiation. The number of total events analyzed for each strain is indicated on the graph. Error bars, mean ± s.e.m.

(G) The frequency of AVE GCaMP activation events does not change in CEPsh-ablated animals, but is reduced by tetanus toxin expression in AVE. Error bars, mean ± s.e.m.; *, $p<0.01$, random permutation test. Number of animals is indicated within or above each bar.

Pausing					
Gene	**Allele**	**FC**	***p* value**	***n***	**ALA**
cat-2	*(e1112)*	1.02	0.9791	4	-
tph-1	*(mg280)*	0.78	0.7832	4	-
eat-4	*(ky5)*	1.23	0.6250	4	0.15
snf-11	*(ok156)*	1.02	0.9591	12	0.37
kpc-1	*(gk8)*	1.11	0.7580	4	-
aex-5	***(gk419962)***	**0.31**	**0.0219**	**13**	**54.5**
egl-3	*(n150)*	1.28	0.3374	4	42
egl-21	*(n476)*	0.79	0.2154	17	55.9
ida-1	*(ok409)*	3.02	0.0011	8	41.3
nlp-8;flp-13;flp-24	*(ok1799);(tm2427);(gk3109)*	1.06	0.8270	10	>332
flp-7	*(ok2625)*	1.35	0.4052	4	4518.55
flp-27	*(tm4612)*	0.45	0.1531	8	40.13
flp-27	*(gk3331)*	2.58	0.0210	8	40.13
npr-22	*(ok1598)*	0.7	0.2503	10	-
npr-1	***(ad609)***	**0.14**	**0.0004**	**10**	**-**
npr-1+ rescue	*(ad609)+(kyEx1966)*	1.39	0.4918	4	

Developmental delay					
Gene	**Allele**	**FC**	***p* value**	***n***	**ALA**
unc-31	*(e928)*	1.15	0.0041	2	-
bli-4	*(e937)*	1.02	0.6280	2	4.23

Supplemental Table S1. Related to Figure 4.

Effect of mutations in neurotransmitter and neuropeptide pathways on CEPsh glia ablation-induced pausing (top), and developmental delay (bottom). FC, response fold change relative to CEPsh glia-ablated animals. *p* value, two tailed student's *t* test. *n*, number of movies analyzed or experimental replicates. ALA, gene expression levels in ALA according in RPKM (Nath et al., 2016).

Experimental Procedures

Strains

C. elegans strains were cultured at 20°C as described (Brenner, 1974), unless otherwise indicated. Wild-type (WT) animals were Bristol strain N2. Other alleles used in this work are:

IB16-*ceh-17(np1)I.* VC48- *kpc-1(gk8)I.* OS8656- *aex-5(gk419962)I* outcrossed x4. OS11077- *nlp-8(ok1799)I; flp-13(tm2427)III, flp-24(gk3109)III.* CB937- *bli-4(e937)I.* PS5131- *let-23(sy12)II.* CB1112-*cat-2(e1112)II.* MT15434- *tph-1(mg280)II.* VC2012- *flp-27(gk3331).* FX4612- *flp-27(tm4612)II* . OS9414-*eat-4(ky5)III* outcrossed x2. OS11752- *ida-1(ok409)III* outcrossed x1. FK234- *egl-4(ks62).* DA521- *egl-4(ad450)IV*. RB1405- *npr-22(ok1598)IV*. MT1071- *egl-21(n476)IV*. DA509- *unc-31(e928)IV* outcrossed x10. RM2710- *snf-11(ok156)V* outcrossed x6. MT150- *egl-3(n150)V* outcrossed x1. RB1990- *flp-7(ok2625)X.*

The following transgenic strains were used:

OS3537- *nsIs168* (P*hlh-17*::recCaspase-3, P*unc-122*::GFP, P*ptr-10*::myrRFP)

OS3549- *nsIs180* (P*hlh-17*::recCaspase-3, P*unc-122*::GFP)

OS3540- *nsIs171* (P*hlh-17*::recCaspase-3, P*unc-122*::GFP)

OS6243- *nsIs168; egl-4(ad450)*

OS6084- *nsIs168; egl-4(ks62)*

PS5803- P*ida-1*::GFP, *pha-1(e2123ts)*

OS4700- *nsIs168;* P*ida-1*::GFP

OS4882- *nsIs171; ceh-17(np1)*

OS4699- *nsIs168; ceh-17(np1)*

OS4762- *nsEx2714* (P*pept-3*::GFP, P*odr-1*::RFP)

OS4884- *nsIs168; nsEx2714*

OS4976- *nsEx2846* (P*pept-3*::TeTX, P*elt-2*::mCherry)

OS4977- *nsEx2847* (P*pept-3*::TeTX, P*elt-2*::mCherry)

OS5015- *nsEx2846*; *ceh-17(np1)*

OS5016- *nsEx2847*; *ceh-17(np1)*

OS6265- *nsEx2941* (P*ver-3*(700bp)::CD4-spGFP11, Coloem::dsRed); *nsEx2943* (P*pept-3*::CD4-spGFP1-10, P*elt-2*::mCherry); *nsEx3485* (P*pept-3*::NLG-1::mCherry, *rol-6(+)*)

OS6039- *nsEx3358* (P*pept-3*::GCaMP2.2, P*unc-122*::dsRed)

OS6261- *nsIs180; nsEx3358*

OS6615- *nsEx3358; ceh-17(np1)*

OS6617- *nsIs180; nsEx3358; ceh-17(np1)*

OS6851- *nsEx3737* (P*pept-3*::TeTX-sl2-GCaMP2.2, P*unc-122*::dsRed)

OS6858- *nsEx3744* (P*pept-3*::TeTX-sl2-GCaMP2.2, P*unc-122*::dsRed)

OS5012- *nsIs168; eat-4(ky5)*

OS3981- *nsIs168; tph-1(mg280)*

OS9880- *nsIs168; snf-11(ok156)*

OS7750- *nsIs168; kpc-1(gk8)*

OS8697- *nsIs168; aex-5(gk419962).*

OS8698- *nsIs168; egl-3(n150)*

OS7401- *nsIs168; egl-21(n476)*

OS11084- *nsIs168; flp-13(tm2427), flp-24(gk3109); nlp-8(ok1799);*

OS7527- *nsIs168; flp-7(ok2625)*

OS7915- *nsIs168; flp-27(gk3331)*

OS8083- *nsIs168; flp-27(tm4612)*

OS7746- *nsIs168; npr-22(ok1598)*

CX9396- *npr-1(ad609); kyEx1966 (*P*flp-21::*NPR-1-sl2-GFP*,* P*ofm-1::*dsRed*)*

OS8085- *nsIs168; npr-1(ad609); kyEx1966 (*P*flp-21::*NPR-1-sl2-GFP*,* P*ofm-1::*dsRed*)*

OS7604- *nsIs168; unc-31(e928)*

OS9400- *nsIs168; bli-4(e937)*

OS11763- *nsIs168; ida-1(ok409)*

Germline transformations were performed as described (Mello and Fire, 1995). Stable transgenes were obtained via psoralen integration (Yandell et al., 1994).

Ablations

Laser ablations of the ALA, AVE and CEP neurons were performed as described (Bargmann and Avery, 1995) in L1 larvae of strains expressing GFP under the *ida-1, pept*-3 or the *dat-1* promoters, respectively, to assist in neuron identification. Ablated animals were selected for the behavioral experiments by absence of GFP. For genetic ablation of CEPsh glia, the two parts of a reconstituted Caspase-3 (Chelur and Chalfie, 2007) were expressed in CEPsh glia starting at the early L1 stage by using the *hlh-17* promoter (McMiller and Johnson, 2005). In all animals tested complete elimination of all four CEPsh glia in these strains was observed based on the lack of P*ptr-10::*myrRFP expression in the CEPsh cells (n>50), and also confirmed in two animals by EM reconstruction.

Analysis of animal locomotion

A day prior to behavior recordings, L4 larvae were picked to a fresh plate with food. The next day, 20-40 adult animals were picked to an unseeded plate, washed three times with M9 buffer, and transferred to a 6 cm plate containing 4 ml of NGM-agar, with a high-osmolarity barrier (4M Fructose) at the periphery of the plate to prevent wandering of animals off the plate. Animals were allowed to adjust to the plate for 20 minutes before the plate was placed under a video camera, and locomotion was recorded for 30 minutes at 2 frame/sec (Movies S1, 2). Animal locomotion was analyzed using custom software written in Java, as follows.

Worm tracking

Individual movie frames are first analyzed separately to determine worm positions. The background of each frame is computed using a median filter (65x65 pixels) and subtracted before further processing. A binary image is then obtained by thresholding; objects in the image are identified as the connected components of the foreground, and define groups of pixels in the background-subtracted image. The total intensity of an object is computed by summing the intensities of its pixels, and its center as the center of mass of its pixels (weighted by their intensities). Objects with a total intensity below a set threshold are discarded.

Objects in two consecutive frames are then matched if they have at least one pixel in common (the frame rate was sufficiently high that images of a worm in two consecutive frames always overlapped). This

defines a “trajectory graph” whose vertices are object centers in the different movie frames and whose edges connect matched objects in consecutive frames. Branches of the graph define candidate worm trajectories, which are then edited, automatically and manually, to remove spurious tracks. Firstly, worms can come in contact as they move around the plate, and occasionally remain alongside one another before they separate. These touching worms are incorrectly identified as a single object. However, encounters between worms are readily detected in the trajectory graph as two incoming branches merging into a single branch. The merged branch is then discarded. Conversely, a single branch that splits into two is identified as two adjacent worms that later separated, and discarded. Another source of spurious tracks are dust particles and damaged or dead worms. These immobile objects are detected as tracks that do not deviate from their average position by more than a threshold distance, and discarded. This automated processing eliminates most spurious tracks, so that limited subsequent manual editing is needed. A graphical interface was developed for that purpose, allowing the user to inspect tracking results and discard incorrect tracks.

Analysis of worm pausing

Worm trajectories were analyzed to identify periods of movement and pausing, according to the variations in worm velocity. To estimate the velocity of a worm, its trajectory is first smoothed by convolution with the kernel

$$h(k) = \frac{3^{-|k|}}{2}.$$

The velocity of the worm between frames k and k+1 is then defined as

$$v_k = \frac{\left\| \vec{r}_{k+1} - \vec{r}_k \right\|}{\Delta t},$$

where $\vec{r}_k$ denotes the position of the worm in frame k and Δt=0.5 s is the interval between frames.

This rapidly decaying kernel is chosen as a compromise between preserving rapid variations in worm velocity and reducing noise in the estimation of worm positions. The velocity of the worm between consecutive frames is estimated as the distance between points in the smoothed trajectory divided by the time interval Δt between frames.

Because pausing worms exhibit some residual movement and the velocity of moving worms can be small (e.g. when they are reversing), these two states cannot be discriminated based on instantaneous velocity; as seen in Figure S1B, the velocity distribution of glia-ablated worms does not have a clear bimodal structure. An improvement over velocity thresholding at each time point would be to require that the velocity remains above/below threshold for a minimum period of time. However, this would require introducing several somewhat arbitrary parameters and would be sensitive to noise. To explicitly allow for ambiguities in the identification of movement and pausing, trajectories were analyzed using a statistical model, specifically a Hidden Markov Model (Press, 2007).

The model, depicted in Figure S1C, comprises two states, moving and paused (denoted *M* and *P*). At each time step, a moving worm can pause with probability p_p and a paused worm can start moving with probability p_m. Thus, if S_k denotes the state of the worm in the interval between frames *k* and *k*+1,

$$p(S_{k+1} = M) = (1 - p_p)\, p(S_k = M) + p_m\, p(S_k = P),$$
$$p(S_{k+1} = P) = (1 - p_m)\, p(S_k = P) + p_p\, p(S_k = M).$$

The velocity of the worm depends on its state, and is assumed to follow a half-normal distribution with scale σ_M and σ_P for the moving and paused states, respectively:

$$p(V_k = v \mid S_k = M) \propto e^{-\frac{v^2}{2\sigma_M^2}},$$
$$p(V_k = v \mid S_k = P) \propto e^{-\frac{v^2}{2\sigma_P^2}}.$$

Note that this simple model is not intended to accurately represent the statistics of worm movement; instead, it formalizes minimal assumptions about movement and pausing, and allows their identification to be cast as an inference problem. That is, given an observed velocity sequence $\mathbf{v} = \{v_1, \ldots, v_n\}$, the model defines a likelihood (posterior probability) $P(\mathbf{s} \mid \mathbf{v})$ for every sequence of model states $\mathbf{s} \in \{M, P\}^n$, e.g. $\mathbf{s} = \{M, M, P, \cdots\}$. The probability that the worm was in the paused state in the interval between frames *k* and *k*+1 is the marginal probability $P(S_k = P \mid \mathbf{v})$. The forward-backward algorithm (Press, 2007) allows efficient computation of the likelihood of state sequences and other quantities of interest, such as the expectations of the time spent in each state and of the number of transitions between the two states. The transition probabilities p_p and p_m can thus be re-estimated from

the output of the algorithm. The Baum-Welch algorithm (Press, 2007; Welch, 2003) iterates rounds of the backward-forward algorithm and parameter re-estimation; the likelihood of the data under the model increases monotonically at each step, guaranteeing convergence to a maximum. Thus, transition probabilities are not free parameters of the model but estimated from the data.

This procedure was used to estimate transition probabilities for each analyzed movie (pooling all the tracks in the movie). On the other hand, the velocity scales σ_M = 150 μm/s and σ_P = 5 μm/s (which could also be re-estimated) were kept fixed for all movies, to ensure a consistent definition of the two states across all experiments; these values were determined from the analysis of a sample of movies of wild-type worms.

Figure S1D illustrates the output of this analysis. Because of the probabilistic nature of the model, transitions between states are not discrete but occur over a small number of time steps. Also, ambiguous features of the activity curve give rise to fractional probabilities. The fraction of the total time animals were found pausing in all tracks relative to the overall duration of all the tracks in a movie was used to calculate the percentage of time adult animals spent pausing.

Lethargus behavior assays

Intermolt and lethargus quiescence assays were performed in "artificial dirt" PDMS chips as previously described (Iwanir et al., 2013), except that mid L4 larvae were picked from a population of mixed stage animals according to their morphology, and behavior was recorded for 10 hours. For the traces in Figure 1A,B , the fraction of quiescence was calculated as described by (Iwanir et al., 2013) over a 10-minute running window. For statistical analysis of populations, the fraction of quiescence was discretely calculated for one-hour bins. Generally, the onset of lethargus was defined as the first time-point from which the fraction of quiescence remained above 5% for 20 consecutive minutes, for animals displaying substantial pre-lethargic quiescence, the starting point for the quiescence threshold search was determined manually based on the quiescence profile.

Statistical significance was tested using one-way ANOVA with Tukey-Kramer Correction on planned comparisons of the double mutants to each parent line, and each parent line to the wild type.

Scoring development

Ten gravid adult animals were allowed to lay eggs for 4 hours and removed from the plate. Animals were scored 55 hours later and placed into three groups, worms that reached adulthood, L4 larvae, and L1-L3 larvae. The percentage of animals in each group was calculated. The data shown is the average of three assays, with at least 150 worms scored in each assay.

Scoring synapses by GRASP

GRASP expressing lines were generated as described (Feinberg et al., 2008). Two individual lines, separately expressing the two parts of CD4-GRASP in ALA and AVE, were crossed together and specific expression of GFP within the nerve ring was confirmed. To verify that these neurons interact at synaptic sites, AVE synapses were marked with neuroligin (NLG-1::mCherry), and the percentage of animals with an overlapping red signal out of a population of animals with a clear GRASP signal was calculated. Fluorescence imaging was done using an Axioplan II microscope equipped with an AxioCam camera, using a 63x/1.4 NA objective. Figures were assembled using Photoshop (Adobe Software).

Calcium imaging

Calcium imaging from AVE neuron was performed using a microfluidic device as described (Chronis et al., 2007). Images were captured at 4 frames/sec and were analyzed using AxioVision 4.7.

Analysis of AVE activity and response

Images were first downsampled (from ≈ 0.1μm/pixel to 0.4μm/pixel) then processed as follows.

Neuron tracking

The location of the neuron in each movie frame is determined as a local maximum of the image after smoothing with a Gaussian filter (standard deviation of 4 pixels ≈ 1.6μm). The initial location is set to the absolute maximum in the first frame (or manually if this does not match the position of the neuron). Subsequently, the location in each frame is determined as the maximum within a distance *r* of the location in the previous frame (the default value of *r* was 32 pixels ≈ 13μm). This procedure tracked the neuron

correctly for the majority of movies, and for most others with the following adjustments. The value of *r* was increased (to 64 pixels) for movies in which motion exhibited sudden jumps (N=4/300). When other structures in the vicinity of the neuron interfered with the tracking, the value of *r* was reduced (to 16 pixels, provided motion was not too fast; N=17/300) and/or possible neuron positions were restricted to a manually defined rectangular area (N=9/300). For some movies, these adjustments were not sufficient to track the neuron correctly. These movies represented a limited fraction of all recordings (N=35/300) and were omitted from the analysis.

Estimation of neuron activity

At each time point, the activity of the neuron is estimated from pixel intensities in a circular area around the estimated neuron position. The radius of the area (20 pixels ≈ 8μm) is chosen to be as small as possible while sufficient to enclose the body of the neuron. The background intensity in the vicinity of the neuron is estimated as the median intensity in a ring-shaped domain with an inner radius of 20 pixels and an outer radius of 40 pixels. Finally, the activity of the neuron is estimated by summing over the inner circular area the pixel intensity minus the background level. For every movie, this value is divided by its time average, yielding a dimensionless measure of neuron activity. Examination of the resulting activity curves suggested variations in measurement noise (due e.g. to variations in imaging conditions). Curves that were deemed too noisy (based on an RMS variation in activity level > 0.1 between successive frames; N=10/265) were excluded from further analysis.

Analysis of neuron activity

Inspection of activity curves obtained for wild-type worms (e.g. Figure S4A) suggests that as was previously reported (Kato et al., 2015) they may be broken down into four states: ramping up, ramping down, and high or low plateaus (denoted *U*, *D*, *H*, and *L*, respectively). As for the analysis of worm locomotion, a Hidden Markov Model (depicted in Figure S4C) was used to classify neuron activity into these four states (here also, the model is not intended to represent the detailed statistics of neuron activity, but as a tool for its analysis).

Because reporter activity and the measurement process are noisy, it is not possible to directly use increments between successive time points to define the four states, unless the activity curves are strongly smoothed. On the other hand, this would blur the transitions between ramps and plateaus. To explicitly allow for uncertainty in the measurement of neuron activity, a hidden variable corresponding to the "true" activity level was incorporated into the model. For the purpose of inference, the range of possible activity levels is discretized into N evenly spaced values, $\{l_1,\cdots,l_N\}$ (N=128 is chosen such that the increment Δl between levels is smaller than the measurement noise). The model thus comprises $4N$ states, corresponding to all possible combinations of activity states (U, D, H, L) and activity levels.

At each time step, the possible transitions between model states include transitions between activity states and transitions between different activity levels. By definition, transitions between ramping up and low plateau are not permitted, as well as transitions between ramping down and high plateau and transitions between plateau states. Thus, if S_k denotes the activity state at time t_k and $p_{A\to B}$ denotes the probability of an allowed transition between activity states A and B,

$$P(S_{k+1}=U)=(1-p_{U\to H}-p_{U\to D})P(S_k=U)+p_{L\to U}P(S_k=L)+p_{D\to U}P(S_k=D).$$

Similar equations are obtained for the other three states.

Variations in the activity level depend on the activity state. By definition of the activity states, activity can only increase in the ramping up state or decrease in the ramping down state. Steps in activity in these two states are assumed to follow an exponential distribution with scale λ, e.g. if L_k denotes the activity level at time t_k,

$$P(L_{k+1}=l_j \mid L_k=l_i, S_k=U)\propto e^{-\frac{l_j-l_i}{\lambda}}.$$

The scale λ can be written as $\lambda=\rho\Delta t$, where ρ is the average rate of change of the activity level and $\Delta t=0.25\text{s}$ is the time step between movie frames.

Activity in the plateau states is assumed to be approximately constant, with small fluctuations only; transitions are allowed only between adjacent levels (among the N bins), with a small probability ε, e.g.

$$P(L_{k+1} = l_{i-1} \mid L_k = l_i, S_k = H) = \varepsilon,$$
$$P(L_{k+1} = l_i \mid L_k = l_i, S_k = H) = 1 - 2\varepsilon,$$
$$P(L_{k+1} = l_{i+1} \mid L_k = l_i, S_k = H) = \varepsilon.$$

This corresponds to a diffusive evolution with diffusivity

$$D = \varepsilon \frac{\Delta l^2}{\Delta t}.$$

Finally, the measurement of activity levels is assumed to be corrupted by Gaussian white noise with a variance σ^2, thus if l_k^{obs} denotes the level measured at time t_k,

$$P(l_k^{\text{obs}} \mid L_k = l_i) \propto e^{-\frac{(l_k^{\text{obs}} - l_i)^2}{2\sigma^2}}.$$

Given an observed activity sequence, $\mathbf{l}^{\text{obs}}$, the likelihood of state sequences, $P(\mathbf{s},\mathbf{l} \mid \mathbf{l}^{\text{obs}})$, is computed using the forward-backward algorithm. The rate of neuron activation is then obtained as the expected frequency of transitions to the ramping up state. Estimation of transition probabilities between activity states using the Baum-Welch algorithm was found to result in over-segmentation (high transition probabilities were obtained, with small jumps in activity being classified as transitions), thus their values were kept fixed. For simplicity, all allowed transitions were assigned the same probability *p*. This and the other model parameters were adjusted to values yielding satisfactory classification: $p = 0.01/\text{s}$, $\rho = 0.4/\text{s}$, $D = 2 \times 10^{-5}/\text{s}$, and $\sigma = 0.08$. Figure S4D illustrates the output of this procedure. As with the model of worm movement and pausing, transitions between states are not discrete but occur over a small number of time steps, and ambiguous features of the activity curve give rise to fractional probabilities (e.g. the shoulder in activity near *t*=90 is partly classified as a high plateau).

Analysis of the response to neuron activity

The above statistical model is well suited to count neuron activations, because there is a continuum from sharp onsets of activity to small jumps due to fluctuations in neuron activity and/or measurement noise. To assess the response of the worm to neuron activation, on the other hand, it is desirable to consider only the clearest activation events. To this end, discrete activation events are identified as time intervals where the

ramping up state has highest probability (among the four activity states), and the amplitude of an event is defined as the change in the measured activity level over the corresponding time interval; only events with an increment in ΔF/F above 0.6 are retained. Also, only those events which follow a low plateau (i.e. the low plateau state has the highest probably immediately before the start of the event) are considered, to ensure that the response to the activation event is separated from the response to prior down-steps in AVE activity. For each line, all events in the analyzed movies are pooled together to compute the average activity and worm position as a function of time (relative to event start time).

As shown in Figure 4B, wild-type worms respond to AVE activation by a sharp backward movement, while the response of glia-ablated worms is much less distinct. The strength of this phenotype is quantified according to the frequency with which worms move backward following neuron activation. To this end, the positions of the worm at two time points are compared. The first is the forward-most position of the worm within 2 seconds after the start of the activation event (this allows for the forward movement of wild-type worms between the start of the event and the onset of the response). The second time point is 8 seconds after the start of the event, corresponding to the typical duration of sharpest backward movement in wild-type worms. The response of the worm is measured by the difference *dx* in position between these two time points, and deemed "correct" or "incorrect" depending on whether the worm has moved backward ($dx < 0$) or forward ($dx > 0$). Because the movement of the worm is measured relative to the forward-most position in a 2-second interval after the start of the event, the resulting estimation of "error rates" is rather conservative: if it is computed using randomly drawn event times, an error rate of about 1/3 is obtained. The strength of the defect is measured relative to this randomized value, thus in the absence of any correlation between AVE activity and movement the defect has a strength of 1.

Plasmids

For specific expression in AVE, we PCR-amplified a 2.5 kbp genomic DNA fragment containing a sequence that ends 240 bp upstream of the *pept-3* ATG (Fei et al., 2000). *Fse*I and *Asc*I restriction sites were added on both sides of this amplicon, respectively. This fragment was ligated to the following vectors digested with the same enzymes: pSM-GFP; pSM-TeTx-mCherry; pSM-GCaMP2.2; pSM-NLG-1-mCherry; pSM-CD4-spGFP1-10.

For specific expression in ALA, we PCR-amplified a 650 bp genomic DNA fragment containing sequences upstream of the *ver-3* ATG (Popovici et al., 2002). The resulting amplicon was ligated to pSM-CD4-spGFP11 vector digested with *Fse*I and *Asc*I.

References

Bargmann, C.I., and Avery, L. (1995). Laser killing of cells in Caenorhabditis elegans. Methods Cell Biol. 48, 225-250.

Brenner, S. (1974). The genetics of Caenorhabditis elegans. Genetics 77, 71-94.

Chelur, D.S., and Chalfie, M. (2007). Targeted cell killing by reconstituted caspases. Proc. Natl. Acad. Sci. USA 104, 2283-2288.

Chronis, N., Zimmer, M., and Bargmann, C.I. (2007). Microfluidics for in vivo imaging of neuronal and behavioral activity in Caenorhabditis elegans. Nat. Methods 4, 727-731.

Fei, Y.J., Romero, M.F., Krause, M., Liu, J.C., Huang, W., Ganapathy, V., and Leibach, F.H. (2000). A novel H(+)-coupled oligopeptide transporter (OPT3) from Caenorhabditis elegans with a predominant function as a H(+) channel and an exclusive expression in neurons. J. Biol. Chem. 275, 9563-9571.

Feinberg, E.H., Vanhoven, M.K., Bendesky, A., Wang, G., Fetter, R.D., Shen, K., and Bargmann, C.I. (2008). GFP Reconstitution Across Synaptic Partners (GRASP) defines cell contacts and synapses in living nervous systems. Neuron 57, 353-363.

Iwanir, S., Tramm, N., Nagy, S., Wright, C., Ish, D., and Biron, D. (2013). The microarchitecture of C. elegans behavior during lethargus: homeostatic bout dynamics, a typical body posture, and regulation by a central neuron. Sleep 36, 385-395.

Kato, S., Kaplan, H.S., Schrodel, T., Skora, S., Lindsay, T.H., Yemini, E., Lockery, S., and Zimmer, M. (2015). Global brain dynamics embed the motor command sequence of Caenorhabditis elegans. Cell 163, 656-669.

McMiller, T.L., and Johnson, C.M. (2005). Molecular characterization of HLH-17, a C. elegans bHLH protein required for normal larval development. Gene 356, 1-10.

Mello, C., and Fire, A. (1995). DNA transformation. Methods Cell Biol. 48, 451-482.

Nath, R.D., Chow, E.S., Wang, H., Schwarz, E.M., and Sternberg, P.W. (2016). C. elegans Stress-Induced Sleep Emerges from the Collective Action of Multiple Neuropeptides. Curr. Biol. 26, 2446-2455.

Popovici, C., Isnardon, D., Birnbaum, D., and Roubin, R. (2002). Caenorhabditis elegans receptors related to mammalian vascular endothelial growth factor receptors are expressed in neural cells. Neurosci. Lett. 329, 116-120.

Press, W.H., Teukolsky, S.A., Vetterling, W.T., Flannery, B.P. (2007). Numerical Recipes: The Art of Scientific Computing, 3rd ed (New York, NY, USA: Cambridge University Press).

Welch, L.R. (2003). Hidden Markov models and the Baum-Welch algorithm. IEEE Information Theory Society Newsletter 53.

Yandell, M.D., Edgar, L.G., and Wood, W.B. (1994). Trimethylpsoralen induces small deletion mutations in Caenorhabditis elegans. Proc. Natl. Acad. Sci. USA 91, 1381-1385.